Rock temperature prior to failure: analysis of 209 rockfall events in the Mont Blanc massif (Western European Alps)

A Legay, Florence Magnin, Ludovic Ravanel

Rock temperature prior to failure: analysis of 209 rockfall events in the Mont Blanc massif (Western European Alps)

A. Legay[1], F. Magnin[1], L. Ravanel[1]

[1] EDYTEM Lab, Université Savoie Mont Blanc, CNRS, Le Bourget-du-Lac, France

Corresponding author: Florence Magnin [florence.magnin@univ-smb.fr]

Key words: rockfall, alpine rockwall, thermal modeling, permafrost, Mont Blanc massif

1   **ABSTRACT**

2   Periglacial rockwalls are affected by an increase in rockfall activity attributed to permafrost

3   degradation. While recent laboratory testing has asserted the role of permafrost in bedrock

4   stability, linking experimental findings to field applications is hindered by the difficulty to assess

5   bedrock temperature at observed rockfall locations and time. In this study, we simulated bedrock

6   temperature for 209 rockfalls inventoried in the Mont Blanc massif between 2007 and 2015 and

7   209 000 random events artificially created at observed rockfall locations. Real and random events

8   are then compared in a statistical analysis to determine the results significance. Permafrost

9   conditions (or very close to 0 °C) were consistently found for all events with failure depth > 6 m,

10   and for some events affecting depths from 3 to 6 m. Shallower events were likely not related to

11   permafrost processes. Surface temperatures were significantly high up to at least 2 months prior to

12   failure with the highest peaks in significance 1.5 to 2 months and 1 to 5 days before rockfalls.

13   Similarly, temperature significances at scar depths were significantly high, but steadily decreasing,

14   1 day to 3 weeks before failure. The study confirms that warm permafrost areas (> -2 °C) are

15   particularly prone to rockfalls, and that failures are a direct response to extraordinary high bedrock

16   temperature in both frozen and unfrozen conditions. The results are promising for the development

17   of a rockfall susceptibility index but uncertainty analysis encourages to use a greater rockfall

18   sample and a different sample of random events.

19

20   **1. Introduction**

21

22   Rockwalls can be affected by significant gravity-related transfers of material throughout rockfall,

23   defined here as the detachment of a mass of rock with a volume exceeding 100 m^3 from a series

24   of discontinuities, and its transportation downslope on variable distance[1]. Rockfall is one of the

25   most hazardous geomorphological processes in Alpine massifs and can threaten mountain

26   infrastructure[2–5], tourism[6,7] and valley floors in case of major events[8–12]. Periglacial rockwalls have

27   been increasingly affected by rockfalls[13–18], notably during summer heatwaves[19,20] and permafrost

28   degradation is thus thought to be one of the main factors responsible for these increasing bedrock

29   destabilizations[21–25]. With the projected degradation of alpine permafrost[26], these hazards will

30   likely become a major threat for mountain communities and a better understanding of the thermal

31   context leading to periglacial rockwall failure is therefore crucial.

32   Laboratory experiments conducted over the past two decades have extensively contributed to

33   understand how thawing bedrock may become unstable. In a first stage, Davies et al.[27] have

34   demonstrated that besides the normal stress, the strength of an ice filled rock joint is a function of

35   its temperature. It decreases with warming and reaches a minimal value at -0.5 °C. Then, Mamot

36   et al.[28] have refined this analysis showing a decrease of ice-filled joint resistance by a range of 64

37   - 78 % when the bedrock warms from -10 to -0.5 °C. Those studies agree with former

38   investigations combining field observations and heat conduction modeling to explain the link

39   between the thawing front propagation and boulder fall in periglacial rockwalls[29]. However,

40   Krautblatter et al.[24] have lately explained that the rupture of ice filled joints may only occur at

41   depth < 20 m while, deeper, warming provokes slow deformation along rock-rock contact,

42   meaning that the rupture of ice-filled joints may only explain relatively shallow events. In addition,

43   laboratory experiments have also pointed out that ice-filled joint alteration may also result of

44   enhanced erosion provoked by water percolation and related advective heat transfer[30]. This is

45   supported by field investigations at rockwall sites showing thawing corridors through geophysical

46   soundings[31] or sudden temperature increase in borehole[32]. Water infiltration and circulation may

47   also cause hydrostatic pressure in ice-sealed fractures that could contribute to rockfall

48   triggering[24,25,33,34] as suggested by observations of water together with massive ice in rockfall

49   scars[20–22]. However, determining the role of hydraulic processes in alpine rockfall triggering is

50   challenging because of the lack of fully coupled thermo-hydro-mechanical numerical models and

51   data for parameterization[33].

52   Despite these limits, the link between rock slope failures and permafrost conditions was confirmed

53   for various events using transient heat conduction models for specific rockfalls[21,22] or through

54   comparison of permafrost map[35] and rockfall inventory[26]. Statistical analysis of climate variables

55   or rock surface temperature evolution also showed a strong link between air temperature anomaly

56   and rockfall occurrence in high mountain[36–38,] while various studies explain that strong thermal

57 oscillations and related cyclic thermal stress or thermal expansion related to heating may cause

58 rockfall in non-periglacial environments[39–41].

59 Despite these advances, observations are generally too sparse or inhomogeneous to draw robust

60 statistical analysis of thermal conditions at depth of bedrock failure, which limits the understanding

61 of the link between rockfall and rockwall thermal dynamics and therefore our capacity to predict

62 rockfalls.

63 Our study proposes to investigate bedrock thermal dynamics prior to rockfall occurrence for 209

64 inventoried events during the period 2007-2015 in the Mont Blanc massif. It uses a 1D transient

65 thermal model[42] simulating temperature-depth profiles at a daily time step. Absolute temperatures

66 simulated at the rock surface and at the depths of rockfall scars prior to failures are presented but

67 the main part of the analysis is based on a statistical approach in order to minimize biases in results

68 interpretation. Our study addresses the following research questions:

69 - Which bedrock temperature conditions or dynamics are the most prone to rockfall

70 occurrence?

71 - Is bedrock temperature experiencing exceptionally high value prior to failure?

72 - Is there a statistical relationship between bedrock temperature and rock slope

73 destabilization?

74 The study aims at verifying the hypotheses that the observed rockfalls are a direct reaction to the

75 intense and exceptional summer heatwaves that occurred over the past summers[43–45], and that

76 thawing permafrost (close to 0 °C) areas are the most prone to rockfalls. In this way, it intends to

77 better define the time-lag between the air temperature signal and the bedrock failure and to explore

78 a possible statistical relationship between air temperature, rock temperature dynamics and failure

79 occurrences that would help to predict such events with weather forecast.

80 **2. Study area and rockfall database**

81 The Mont Blanc massif (MBM; Fig. 1), with its highest point at 4809 m a.s.l., is a crystalline

82 massif that extends over an area of 550 km^2 in the Western Alps. It presents two main lithological

83 units: a Variscan metamorphic series in the W and SW of the massif, and an intrusive late-Variscan

84 granite in the central and eastern parts, crosscut by three main sets of shear zones and faults[47].

85 27 % of the massif was covered by glaciers in the 2000s[48], and 7-12 % of the MBM area are

86 permafrost-affected rockwalls[49]. Permafrost is largely present above 2600 and 3200 m a.s.l. on

87 north- and south-facing slopes, respectively[49].

88 In the MBM, infrastructures (cable cars, mountain huts, rack railways[3]) and mountaineers[7] are

89 exposed to rockfall. Rockfalls are surveyed since 2007 by a network of observers[50] focused on the

90 central part (57 %) of the MBM. First based on the use of reporting sheets, the transmission of

91 information is now done more directly (oral communication, telephone, mail) or by using an app.

92 The network of observers is reactivated annually (through articles, meetings, forums, mailing-lists)

93 while amateur climbers are also solicited through posters installed in huts or articles in the

94 specialized press and forums. During each fall, extensive fieldwork is routinely carried out to

95 verify the observations from the network and/or to complete them with further data. In little-visited

96 areas of the mountain range, fieldwork is carried out at locations that were not reported by the

97 network, but identified by correlative deposits. Finally, for each event, the date of occurrence (or

98 observation of the deposit), the precise location of the scar, topographic parameters of the

99 destabilized area (altitude, orientation, slope), the fallen volume, and an estimate of the depth of

100 detachment are documented.

101 Among all the events inventoried between 2007 and 2015, we selected the 209 rockfalls with all

102 required input data for modeling: coordinates, scar depth, date of failure and MARST (Mean

103 Annual Rock Surface Temperature). The MARST was extracted at rockfall locations from the 4-

104 m-resolution map created by Magnin et al.[35]. This map is based on a statistical model calibrated

105 by Boeckli et al.[51] using MARST measurements from the European Alps, computed potential

106 incoming solar radiation and modeled air temperature.
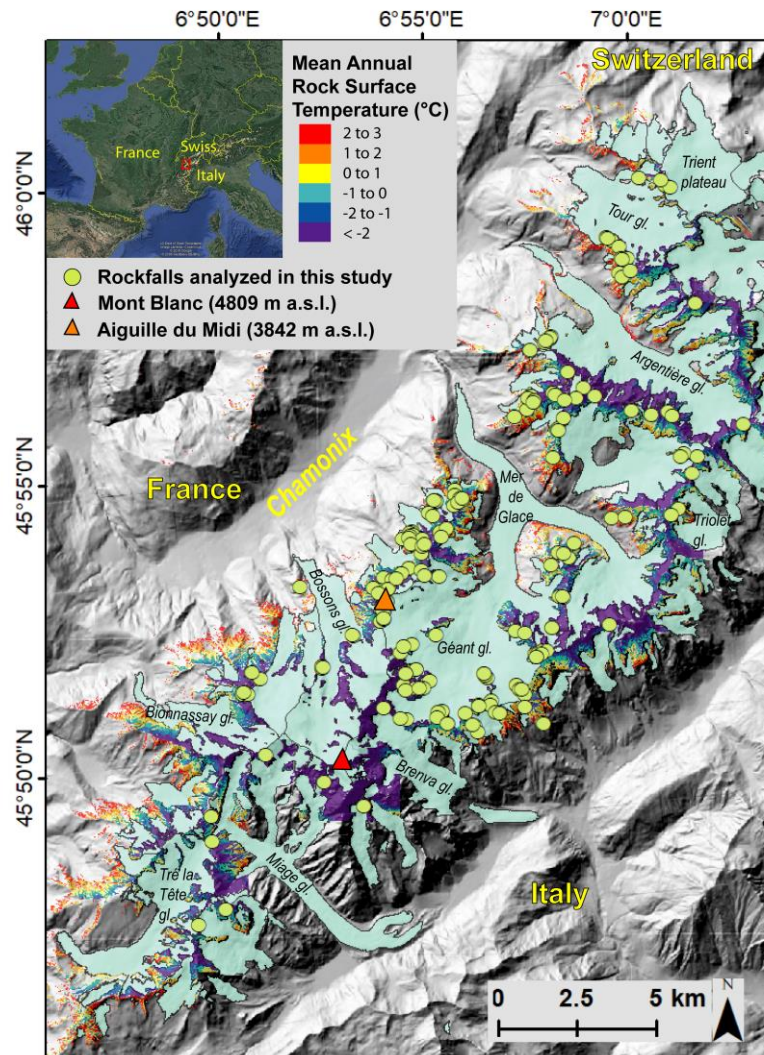
107

108 **Figure 1**. The Mont Blanc massif, the MARST distribution and the location of rockfalls analyzed in this study.

109

110   Summary characteristics of this rockfall database are displayed in Table 1 and their distribution

111   displayed in Figure 1. The detailed characteristics are provided in Table S1. About 5% of the

112   rockfalls (10 events) have a MARST > 2 °C, meaning that they are likely in non-permafrost

113   conditions. Indeed, according to Hasler et al.[52], permafrost might be found below MARST up to

114   3 °C due to the cooling effect of shallow snow cover and air ventilation into fractures. But since

115   the MARST map is built upon mean air temperature for the period 1961-1990 which was about

116   1 °C cooler than the recent period[35], we assume that permafrost may exist below MARST up to

117   2 °C. In addition, 23 events (11%) have MARST between 0 and 2 °C and are thus likely in

118   discontinuous and/or warm permafrost conditions.

119

120   **3. Methods**

121   The goal of our research was to model a temperature-depth (T_z) profile at rockfall locations in

122   order to assess the thermal conditions prior to failure. The simulations were conducted in 1D and

123   intended to represent bedrock temperature perpendicular to the rock surface (Fig. 2). In steep alpine

124   rockwalls, temperature at depth is partly driven by lateral heat fluxes induced by the topographical

125   settings which provoke high surface temperature variability[53]. Thus, we developed an algorithm

126   which accounts for possible lateral heat fluxes in order to correct the modeled T_z profile. In this

127   section, we introduce the so-called CryoGRID2 model (sect. 3.1) that we used to simulate heat

128   transfer, the forcing data and bottom heat flux correction algorithm (sect. 3.2), the model fitting

129   approach (sect. 3.3), the uncertainty calculations (sect. 3.4), and the model implementation at each

130   rockfall location (sect. 3.5).
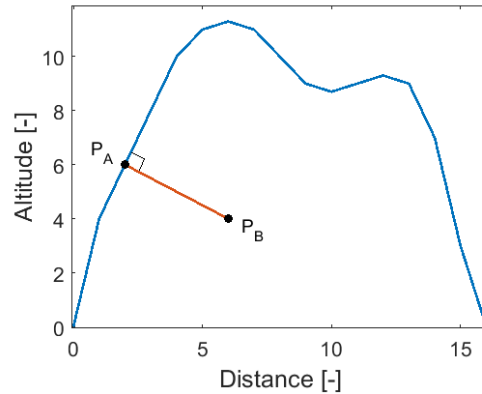
Figure 2. Simplified sketch illustrating the modeled T_z profiles. The blue line represents a topographical profile. P_A is the surface point where the rockfall occurred. P_B is the bottom point of the profile. The red line is the profile where the temperature was calculated at chosen spatial and temporal steps. Altitude and distance are in arbitrary units.

3.1. Heat diffusion modeling with CryoGRID2

We used CryoGRID2 for simulating T_z profiles, a MATLAB diffusive transient thermal 1D model developed by Westermann et al.[42] solving a nonlinear diffusion equation over time. Initially developed for permafrost issues, it solves the conductive heat transfer by taking into account rock properties, air content, water/ice content, and related thawing/freezing processes through latent heat consumption and release. The top of the profile was forced by a surface temperature time series (Dirichlet condition). At the bottom, the profile was forced by a thermal flux (Neumann condition). At every time step, the profile at time n-1 was used as an input for calculating spatial derivatives. At the first time step, we derived an initialization profile by taking the steady state approximation of the equation with the mean of the surface temperature time series for the Dirichlet condition and the first thermal flux for the Neumann condition. This first thermal flux is derived by assuming that the temperature of the profile bottom is equal to the mean of the surface temperature time series (sect. 3.2). CryoGRID2 can handle snowpack at the rock surface. However, since it is almost impossible to construct or obtain such data in steep alpine rockwalls

150   where snow depth is highly variable, snow was neglected in the present study. A summary of the

151   CryoGRID2 principal input parameters and outputs are available in Supplements (Table S2).

152

153   *3.2.   Forcing data and correction heat flux*

154   The top of the T_z profiles was forced with Rock Surface Temperature (RST) time series derived

155   from the summation of an air temperature anomaly to the MARST extracted at rockfall locations

156   (sect. 2). The air temperature anomaly was calculated in comparison to the 1961-1990 mean air

157   temperature used to derive the MARST map (sect. 2) and from the daily air temperature recorded

158   by *Météo France* at Chamonix (1042 m a.s.l.) since 1993 (beginning of hourly air temperature

159   records), similarly to Magnin et al.[26].

160   We created a correction flux applied at the profile bottom (Neumann condition) to account for

161   possible lateral heat fluxes coming from surrounding rock faces by using the MARST map (Fig.

162   1), the 4-m-resolution DEM used to map the MARST and the Chamonix air temperature anomaly

163   time series. We first searched for all surrounding rock faces that may influence the heat fluxes at

164   P_B (see Fig. 2 for P_B) as detailed in the Supplement S1 to obtained N points $(P_i)_{i \in [1:N]}$ at similar

165   altitude than P_A and which were assumed to influence the lower part of the modeled T_z profile

166   (Fig. 3).

167
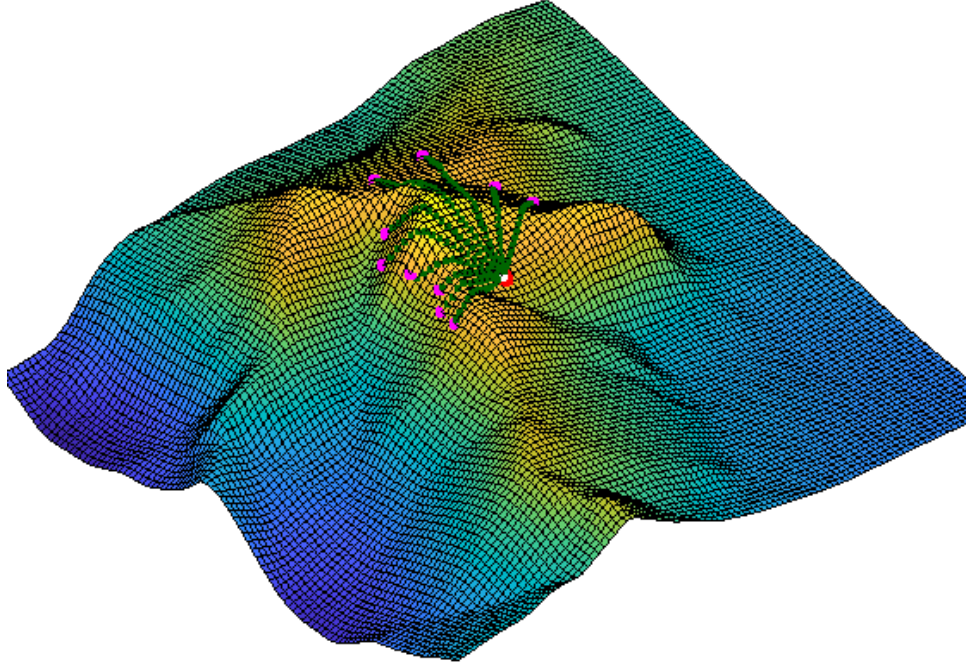
168

169   **Figure 3**. Illustration of the searching method. The 4-m-resolution DEM is represented on a 200×200 m square that

170   contains a 200 m radius circle research limit. The white dot in the center is the surface point P_A (see Fig. 2 for P_A)

171   which is the top of the T_z profile. The red dots surrounding P_A represent all the directions eliminated at the first r-step

172   (see Supplement S1). The green dots represent the research directions. Finally, the magenta dots are the selected points

173   for the correction heat flux calculation. Units and the scale are intentionally hidden to lighten the figure. Likewise,

174   only 20 different directions are plotted (instead of 100 used in this study) to help the readability.

175

176   We then applied thermal fluxes coming from the selected points. For every point P_i, the MARST

177   at P_i location ($MARST_i$) is extracted from the map and distance d_i between P_i and the bottom point

178   P_B of the modeled T_z profile was calculated. For calculating the ith flux, we separated two cases

179   according to d_i ($>$ or $<$ to 30 m) as detailed in the Supplement S1.

180   We thus determined the thermal flux $j_{Q,i}(t)$ of all P_i and calculated the global $j_Q(t)$ as follows:

$$j_Q(t) = c_{exp} \frac{\sum_{i=1}^{N} j_{Q,i}(t)}{100} \qquad (1)$$

181   We divided by 100 because we explored 100 directions, the final flux being an equivalent of a

182   discrete integral. All the fluxes had different directions and different application surfaces. However,

183   we applied all of them at P_B. For considering that, we corrected the final flux by an experimental

184   coefficient c_{exp}. This coefficient was fitted at the same time as the other model parameters (sect.

185   3.3).

186

187   *3.3. Model fitting*

188   The simulated transient temperature fields are affected by a set of parameters related to bedrock

189   properties and model characteristics (Table S2). Principal parameters are listed below and have

190   been fitted by running a host of test values until a minimal difference between simulated and

191   measured temperature profiles into boreholes was achieved.

192   •   The rock thermal conductivity ($k_{bedrock}$), the rock volumetric heat capacity ($c_{bedrock}$), the

193   porosity (φ) and the total water content ($\theta_{w,tot}$), which can be assimilated to the bedrock

194   saturation, all change the soil thermal diffusivity, *i.e.* the time needed for the rock to reach

195   thermal equilibrium.

196   •   Van Genuchten parameters (S2) θ_r, α and n change the (θ_{sat},T) curve. The exact influence is

197   not detailed here but, for example, a higher α will impact the dynamics by requiring a higher

198   temperature for melting all the ice.

199   • c_{exp} changes the magnitude of the lateral heat fluxes (sect. 3.2). For example, the higher is c_{exp},

200   the stronger is the cooling effect of opposite north faces on south faces and *vice versa.*

201   •   Spin-up parameters change the accuracy of the results during the first years of simulation. Tests

202   we performed showed that three years of spin-up are enough for limiting errors under 0.1 °C

203   the first year of simulation and that this error quickly decreases over time.

204   Borehole temperature measurements used for model fitting were collected at the Aiguille du Midi[15]

205   (ADM; 3852 m a.s.l.; Fig. 1). Three 10-m-deep boreholes have been drilled in 2009 in SE, NE and

206   NW-exposed rock faces with varying slope conditions (55 ° to sub-vertical) and snow deposits

207   (from continuous and rather thick to discontinuous and thin snow cover, or very local snow

208   deposit). The NE and NW exposed boreholes (respectively BH_E and BH_N) have been equipped

209   with 15 thermistor-chains spread between 0.3 and 10 m depth, while the SE exposed borehole

210   (BH_S) has 14 sensors spread between 0.14 nd 9.64 m depth. They have been recording

211   temperature since December 2009 (except BH_E: April 2010) at a 3-hour time interval. Model

212   fitting was performed at a daily time step using temperature time series at the shallowest depths as

213   forcing temperature time series at the top of the model domain. The simulated T_z profiles were

214   then compared with measured temperatures in the boreholes.

215   Minimization of the Root Mean Square Error (RMSE) between simulations and boreholes time

216   series were obtained with parameter values displayed in Table 2. Figure 4a displays a simulated

217   T_z profile for a 9 years period with the best-fitted bedrock properties while Figure 4b displays the

218   difference between the measured and the modeled temperature (interpolated between sensors).

219   Figure 5 presents the error distribution obtained with the parameters displayed in Table 2. All the

220   normality tests (Anderson Darling, Kolmogorov Smirnov, Lilliefors…) rejected the hypothesis

221   that this distribution came from a normal distribution at a 5 % significance level. However, the

222   number of points was abnormally high because all the points at every depth and every time were

223   considered in the three cases (more than 5 million points in total). But in reality, there were only

224   three "real" points of comparison (*i.e.*, the three boreholes). The Kolmogorov Smirnov statistic

225   was 0.039 and the critical value corresponding at three data points at a 5 % significance level was

226   0.71, while the critical value with all the points was 10^{-4} order of magnitude. Therefore, in this

227   context of three "real" points of comparison, the test could not reject the hypothesis that the data

228   came from a normal distribution. Thus, for working with Gaussian uncertainties, we assumed this

229   hypothesis of Gaussian errors and we used the mean error of 0.295°C and the standard deviation

230   (σ) of 0.515 °C (Fig. 5) for our analysis. Based on these results, we systematically removed 0.3 °C

231   (upper bound of 0.295 °C) to the final modeled temperatures and a standard deviation value

232    $\sigma_{Cryogrid}$ = 0.55 °C (upper bound of 0.515 °C) was considered for uncertainty (as a reminder, σ

233   corresponds to a 68 % reliable level and 2σ to a 95 % reliable level for Gaussian data).

234
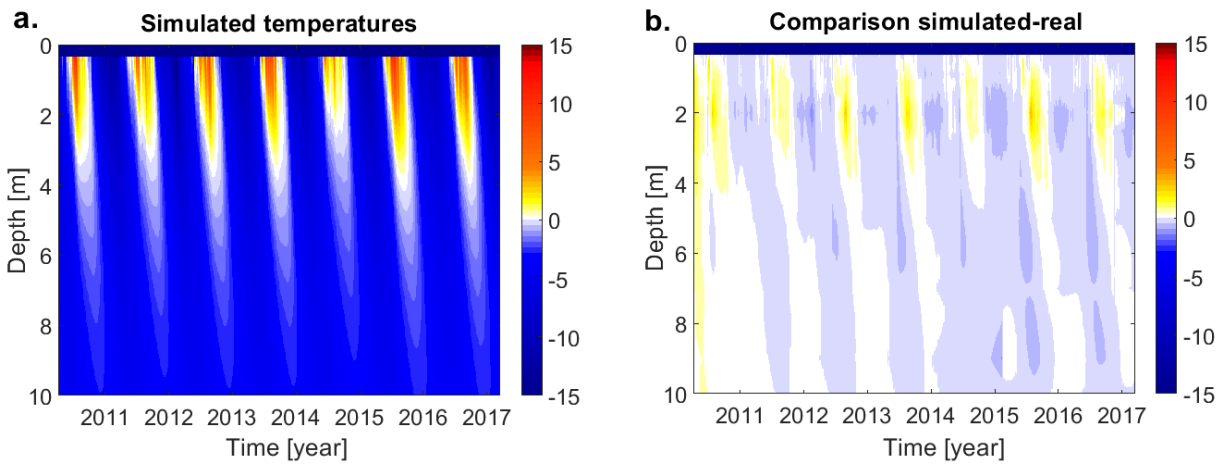
236   **Figure 4. a.** BH_E borehole simulation realized with parameters detailed in Table 2. Input surface temperatures were

237   extracted from the borehole real values. The 0.3 m spatial shift at the top of the profiles is due to the depth of the first

238   temperature value recorded in the borehole. **b.** Comparison between BH_E borehole simulation and real BH_E

239   borehole values. RMSE can then be displaced from these values $(e_i)_{i\in[1:N]}$ by the following formula: $RMSE = \sqrt{\frac{\sum_{i=1}^{N} e_i^2}{N}}$.

240

241
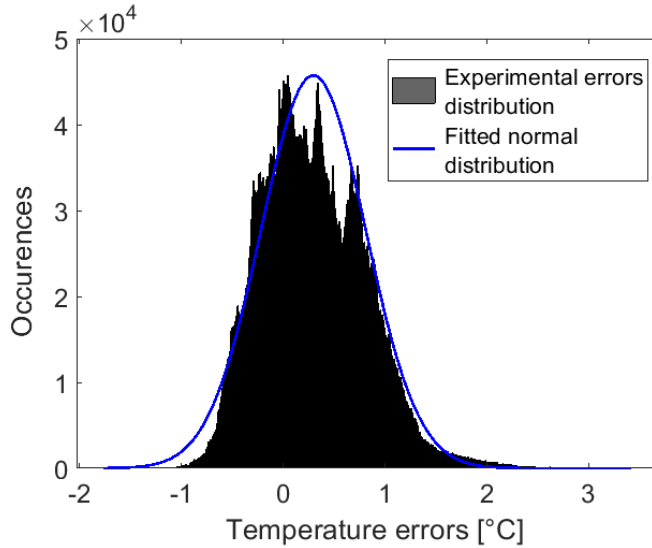
Figure 5. Fit of the temperature errors by a normal distribution. Errors are defined as the difference between the
simulated borehole temperatures (BH_S, BH_E or BH_N) and the real borehole temperatures. The fit gave a mean of
0.295 °C and a standard deviation of $\sigma = 0.515$ °C.

245   *3.4. Uncertainty analysis*

246   In addition to the uncertainty associated with model parameters, the uncertainty of the forcing RST

247   time series must be considered. RST time series being created as the summation of a MARST and

248   anomaly values (see sect. 3.2.), we consider two terms for this uncertainty, one for the MARST

249   and one for the anomalies. For the MARST, the standard deviation of 1.616 °C is reported in the

250   study from Boeckli et al.[51] that describes the statistical model on which is based the initial MARST

251   used in our study (displayed in Fig. 1). We thus kept the upper bound of this value to determine

252    $\sigma_{MARST} = 1.7$ °C. For the anomalies, the uncertainty results from the only consideration of the air

253   temperature changes in Chamonix to create RST anomalies while daily RST variations may also

254   result of the varying lapse rate, which is typical of alpine environments[54], as well as the varying

255   incoming solar radiation and possible snow accumulation[49] which are neglected. We calculated

256   the uncertainty for RST anomalies, referred as $\sigma_{anomaly}$, by using a set of measured RST time series

257   at 5 sensors installed at the top of the ADM in sub-vertical S (2 sensors), N, E, and W exposed

258   rock faces, at a depth of 0.03 m[49].

259   One of the two S-exposed sensors is located right above a ledge where snow accumulates during

260   winter which lowers the MARST by about 1°C compared to snow-free conditions for similar sun-

261   exposure[49]. RST have been recorded continuously at an hourly time step from 2007 to 2010. The

262   MARST for the years 2007 to 2010 were then calculated for each sensor and were adjusted to the

263   1961-1990 period by applying the air temperature anomaly between 1961-1990 and the years of

264   measurements (2007 to 2010). Then, the adjusted MARST of each sensor was subtracted to the

265   measured daily RST to obtain daily temperature anomalies at sensor locations.

266   Comparison between the daily air temperature anomalies measured in Chamonix and the RST

267   anomalies calculated from the 5 RST sensors resulted in Gaussian errors with a standard deviation

268   of $\sigma_{anomaly} = 4$ °C.

269   To sum up, the uncertainties were as follows:

270   • $\sigma_{Cryogrid} = 0.55$ °C

271   • $\sigma_{MARST} = 1.7$ °C

272   • $\sigma_{anomaly} = 4$ °C

273   Then, for surface temperature series, the total uncertainty was:

$$\sigma_{surf} = \sqrt{\sigma_{MARST}^2 + \sigma_{anomaly}^2} \qquad (2)$$

274   Numerically, it gave: $\sigma_{surf} = 4.4$ °C.

275   In the next part of the study, the temperature at the depth of the rockfall scar was analyzed (referred

276   hereafter as "scar temperature"). With most scar depth > 1 m (Tab. 1), these temperatures were not

277   significantly affected by daily surface temperature changes. Thus, $\sigma_{anomaly}$ was neglected when

278   dealing with scar temperatures and total uncertainty for scar temperature was therefore:

$$\sigma_{scar} = \sqrt{\sigma_{Cryogrid}^2 + \sigma_{MARST}^2} \qquad (3)$$

279   Numerically, it gave: $\sigma_{scar} = 1.8\ °C$.

280   To analyze the results, we also used temperature percentiles (sect. 4). A X % temperature

281   percentile is defined as a value which is warmer than X % and colder than (100-X) % of some

282   chosen reference temperatures which were defined as explained in section 4. To estimate modeled

283   temperature percentile uncertainties, simulations were done for the three boreholes, using the

284   MARST map (Fig. 1) and the air temperature anomaly to generate the forcing surface temperature

285   time series. Percentiles of the modeled temperature values were then calculated for the full

286   borehole time series and compared with the real temperature percentile values. Gaussian errors

287   were obtained, with $\sigma_{surf\ prct} = 13.8\ \%$ and $\sigma_{scar\ prct} = 10.7\ \%$. This approach of considering all the

288   uncertainty sources at once was less precise but sufficient in that case with long and complex

289   calculations.

290

291   *3.5. Approach for simulating the temperature dynamics at rockfall locations*

292   To analyze bedrock thermal dynamics prior to rockfalls, the following protocol was used

293   for every event:

294   •   The rock surface temperature time series was created as described in section 3.2.

295   •   The CryoGRID2 simulations were run between 1st January 1993 and 31st December 2015,

296   with the bedrock parameters determined after fitting (Tab. 2). Given that the fitting step

297   showed that a spin-up period of 3 years is sufficient, we assumed that the years 1993-1996

298   were the spin-up years while rockfalls are only documented since 2007. The simulated T_z

299   profiles were 20.5 m long, which is 5 m deeper than the deepest scar depth (Tab. 1). This

300   5 m buffer permitted to lower the errors in the deeper part of the profiles where the

301   correction thermal flux was applied (see sect 3.3).

302 This process was entirely automated in Bash language and MATLAB programs on the Univ.

303 Savoie Mont Blanc - CNRS/IN2P3 MUST computing center. Then, all the simulations could be

304 started at the same time on different calculation resources.

305

306 4. **Approach for result analysis**

307   *4.1. Model output processing and analysis*

308 Four rock temperature variables were analyzed: the (i) scar and (ii) surface temperatures, and the

309 (iii) scar and (iv) surface temperature percentiles. They were all examined through 11 different

310 temporalities: 1 day, 3 days, 5 days, 1 week, 10 days, 2 weeks, 17 days, 3 weeks, 1 month, 45 days

311 and 2 months. The surface temperature was simply extracted at the uppermost depth of the T_z

312 profile (0.05 m). The scar temperature was extracted at the scar depth specified in the rockfall

313 database for each event (Tab. 1). For temporality of 1 day, surface temperature percentiles were

314 calculated by comparing the simulated surface temperature at the day of rockfall occurrence with

315 all the daily surface temperatures of the simulated time series (1st January 1996 - 31st December

316 2015). For other temporalities of *n* days prior to rockfall occurrence, the reference temperatures

317 were calculated by averaging the temperature between a day *d1* which is, by turns, each day in the

318 temperature time series, and a day *d0* which is the first day of the averaging period prior to *d1*,

319 defined as $d0 = d1 - n + 1$. Then, the average temperatures for the various temporalities prior to

320 failure were compared with the respective reference temperatures. At this step, we had only

321 absolute values of surface and scar temperatures, and absolute values of surface and scar

17

322   temperature percentiles. We then aimed at answering if this temperature value was abnormally

323   high for the current period.

324   To do so, 1000 dates were drawn randomly and the 4 studied variables were extracted for the 11

325   different temporalities at each rockfall location. The choice of the number of random events was

326   based on a compromise between the calculation resources and the potential to reduce the

327   uncertainty. The scar depths of the 1000 random dates of a specific event location were chosen

328   equal to the scar depth of this event. To remove sources of biases, dates of the random events were

329   drawn: a) after 2007 and b) with the same monthly distribution as the 209 rockfalls events. Reason

330   for a) was to remove biases linked to the recent decades of atmospheric warming as the rockfall

331   database starts in 2007. If artificial rockfall events would have been drawn in the full period 1996-

332   2015, extracted temperatures at the beginning of the time series would have been expected to be

333   lower and it would have been impossible to determine if a significance of warmer temperatures

334   for rockfall events was real or just related to the atmospheric warming contribution. Reason for b)

335   is that rockfalls mostly occurred between June and October (with an attendance peak in August,

336   Fig. 6a) and these months were, on average, warmer than other months of the year. If random

337   events would have been drawn in the full year, a significance of warmer temperature for real events

338   could have been simply interpreted as the reflection of this reason and not as an extraordinary

339   thermal state of the rock before the failure. Thus, random events were drawn according to the same

340   monthly distribution as the 209 real events (Fig. 6a). Figure 6b shows that the temporal distribution

341   of rockfall events is not dependent on the scar depth, that is why the same monthly distribution is

342   taken for every scar depth and that no scar depth groups were created. Likewise, no relationship

343   was found with the elevation, the slope angle or the sun-exposure (Fig. S1).

344
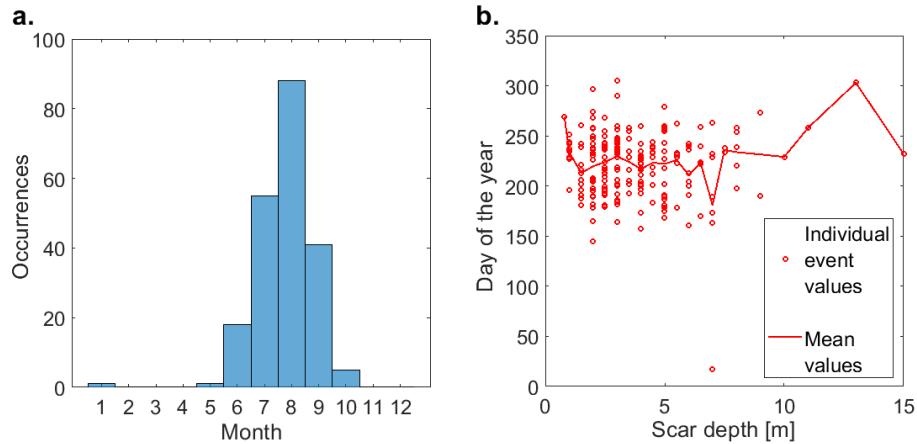
Figure 6. a. Histogram illustrating the distribution of the 209 rockfalls throughout the year that was used as a basis to draw random events dates. **b.** Plot illustrating the distribution of the events throughout the year in comparison to the scar depths. The absence of relationship between scar depth and rockfall timing was considered to not draw the monthly distribution of random events according to depth. The same is true for elevation, slope angle and sun-exposure (Fig. S1). Means of 0.8 m, 9 m, 10 m, 11 m, 13 m and 15 m scar depths must be observed carefully because they are represented by one or two points only.

4.2. *Determining results significance*

For searching significant results, real rockfalls temperatures and temperature percentiles were compared with those of random events. Firstly, a simple comparison of the means for every scar depth and every temporality was realized. Then, the comparison was done for every temporality without regarding the scar depth. Uncertainties were derived by dividing the uncertainty of the variable (σ_{surf}, σ_{scar}, $\sigma_{surf\ prct}$ or $\sigma_{scar\ prct}$) by the square root of the total number of points used for calculating the mean. Since 209 000 random events were considered, uncertainties of the means of random events variables were small and almost impossible to see when plotted against the real events uncertainty.

362   A Kolmogorov Smirnov test (KS test) was then performed for assessing if the real rockfalls sample

363   could have been drawn from the random events distribution. It was calculated by determining the

364   highest ordinate difference between the Cumulative Distribution Functions (CDFs) of the real

365   rockfalls and the random events series. This statistic was then compared with tabulated critical

366   values for obtaining the result of the test. This test was chosen because it is non-parametric, which

367   is important since the temperature percentiles are clearly not Gaussian (Anderson Darling,

368   Kolmogorov Smirnov and Lilliefors tests reject this hypothesis with a 5 % significance level), and

369   because it was possible to consider the uncertainty values while performing the test. This second

370   point is, astonishingly and unfortunately, uncommon for statistical tests. The only feasible rough

371   uncertainty incorporation is generally to present upper and lower bounds of the test by realizing it

372   with the high and low values of the data points. Here, for surface or scar temperature percentiles,

373   the uncertainties were included as explained in the Supplement S2.

374   An example of CDF represented with the uncertainties and resulting KS test is displayed in Figure

375   7 for one specific variable (surface temperature percentile) and one specific temporality (1 day).

376   The KS statistic must be compared with the critical value (cv). If the statistic is higher, the test

377   rejects the hypothesis that the experimental data (real events) comes from the model (random

378   events) with a 5 % significance level. Here, the test rejected the hypothesis that the experimental

379   data (real events) came from the model (random events) in the normal case with a 5 % significance

380   level, but could not reject this hypothesis when considering the uncertainties.
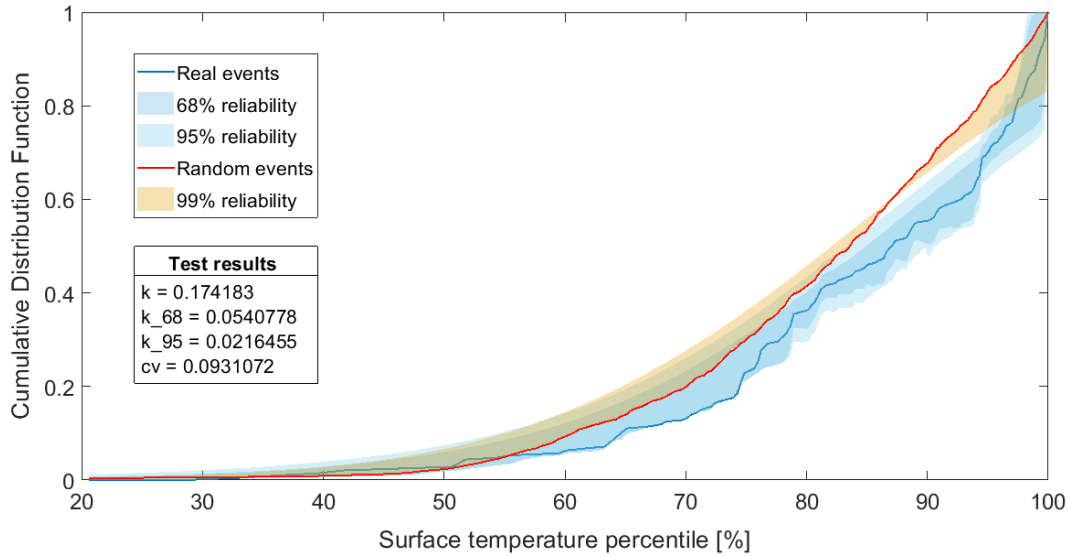
381

382   **Figure 7.** Illustration of a KS test result. The surface temperature percentiles were here considered at the rockfall

383   event day (temporality of 1 day). "k" represents the KS statistic between the CDFs without considering the

384   uncertainties. "k_68" represents the statistic between the 68 % reliable real events CDF and the 99 % reliable random

385   events CDF. "k_95" represents the statistic between the 95 % reliable real events CDF and the 99 % reliable random

386   events CDF. The 68 % and 95 % reliable random events CDFs are not presented because they were very close to the

387   99 % reliable one (the reason for this stability is that random events CDF is made of 209 000 points). "cv" is the 5 %

388   significance level critical value of the KS test in this context. To know the result of the test, the KS statistic must be

389   compared with the critical value. If the statistic is higher, the test rejects the hypothesis that the experimental data (real

390   events) come from the model (random events) with a 5 % significance level. Here, the test rejected the hypothesis in

391   the normal case but could not reject it when considering the uncertainties.

392

393   To show orders of magnitude of simulated temperatures, scar and surface temperature variables

394   were used in a first step. However, in a second step, only temperature percentile variables were

395   kept since they are better for finding statistical significance.

396

397

398   **5. Results**

399   When considering the uncertainties, none of the four variables (surface and scar depth

400   temperatures and temperature percentiles) could be distinguished from the random events values

401   when reasoning by scar depth. This finding is illustrated in Figure 8 for a temporality of 1 day

402   while other temporalities, showing similar patterns, are displayed in the Supplements (Fig. S2).

403   However, whatever the considered variable, the mean distributions were in most cases - except 6

404   and 7 m depths - higher than the random events. This was particularly pronounced for the

405   percentile variables. The four variables were strikingly scattered, but some notable patterns could

406   be distinguished. First, the closer to the surface, the warmer was the scar temperature, for both real

407   and random events. The average temperature became negative from 3-4 m depth downward (see

408   Fig. S2 also) but consistency in negative scar temperature was found for depths > 6 m only, despite

409   a few events showed positive and close to 0 °C conditions. Only 2 events had scar temperature $<$

410   -5 °C. The surface temperatures were mostly positive and no distinct pattern could be found

411   according to scar depths. Scar temperature percentiles scattering increased with depth and their

412   mean decreased from 90 to 50 % between 1 and 9 m depth while surface temperature percentiles

413   showed no obvious link with scar depths. When extending the temporalities (Fig. S2), very similar

414   patterns were found, with slightly smaller scattering, slightly higher surface percentiles and

415   slightly lower scar temperature percentiles.

416
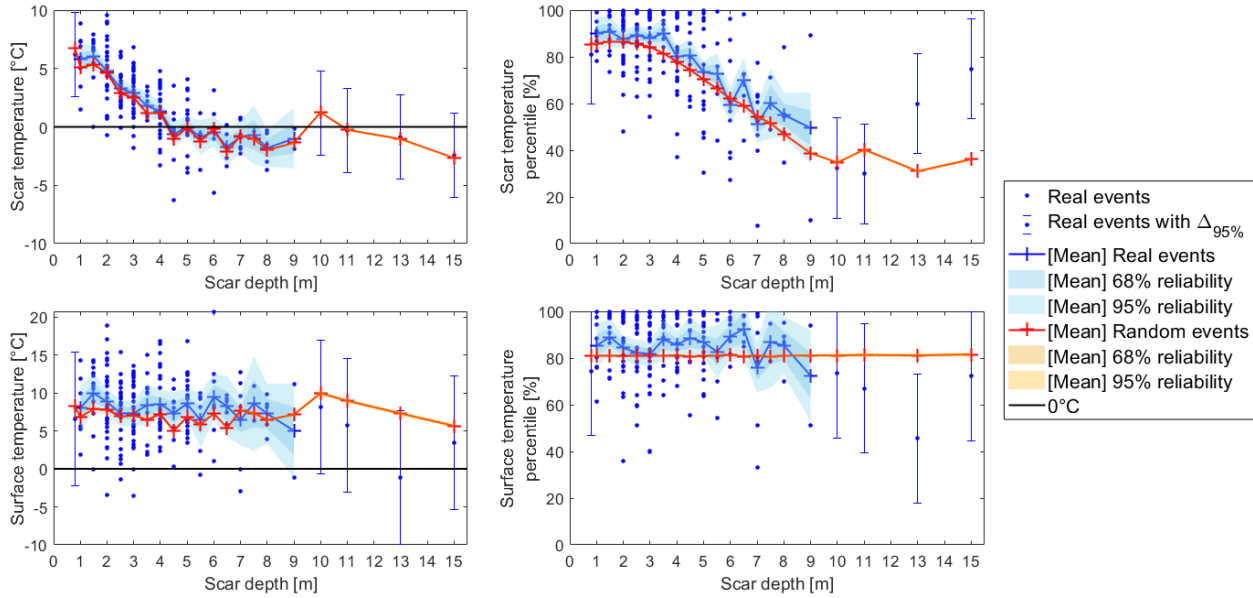
Figure 8. Comparison of the four studied variables between real and random rockfalls on the day of the event (temporality of 1 day). This comparison was done for every scar depth, all the events with the corresponding value of scar depth being used for calculating a mean. Ten other groups of figures like this one were done to verify our results for the 10 other temporalities (3 days, 5 days, 1 week, 10 days, 2 weeks, 17 days, 3 weeks, 1 month, 45 days and 2 months) and four of them (1 week, 2 weeks, 1 month and 2 months) are presented in the Supplements (Figures S2). Uncertainties of random events variables cannot be seen because they were really low (order of magnitude of some degree tenths for temperature variables and some percent tenths for temperature percentile variables).

When looking at the results through the different temporalities, percentiles of scar and surface temperatures were, distinctively higher than the random events values, whatever the temporality (Fig. 9). For scar temperature percentiles, this difference was in order of magnitude of 3 % for mean values and at least 1.5 % for 95 % reliability values. For surface temperature percentiles, these percentages were nearly equal to 2.5 and 0.5 %.

432
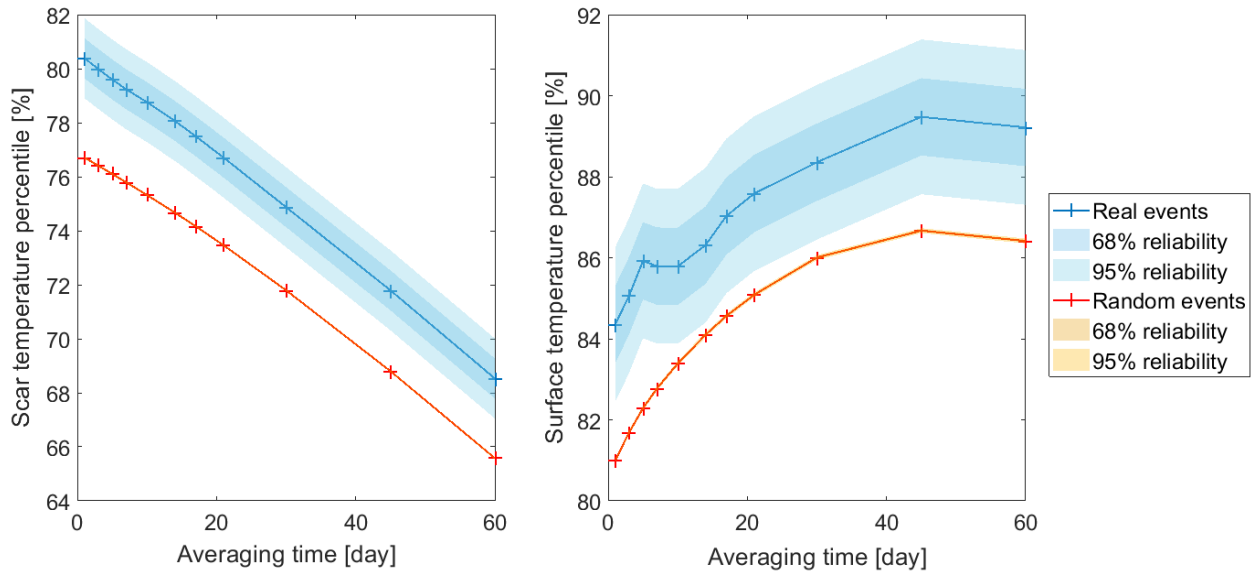
Figure 9. Comparison of the average temperature percentile variables between real and random rockfalls. Here, all scar depths were merged which explains a constant and rather low uncertainty (individual uncertainty divided by the square root of the total number of events, 209 for the real ones and 209 000 for the random ones). Every single point of this represents a full plot of Figure 8.

437

Implementation of the KS test showed that scar temperature percentiles for real events were significantly different from random events for temporalities between 1 and 21 days (Fig. 10). This significance decreases almost continuously with increasing temporality. Surface temperature significances varied with the different temporalities but were always well above the critical threshold. It reached its minimum value at about 14 days averaging time prior to failure and then increased continuously until 45 days averaging time prior to failure where it reached its maximum value. However, when considering the uncertainty, these results were not significant and it was therefore not possible to state whether the real events sample could have been drawn from the random events distribution. This points out the interest to work with a greater number of rockfalls.

447
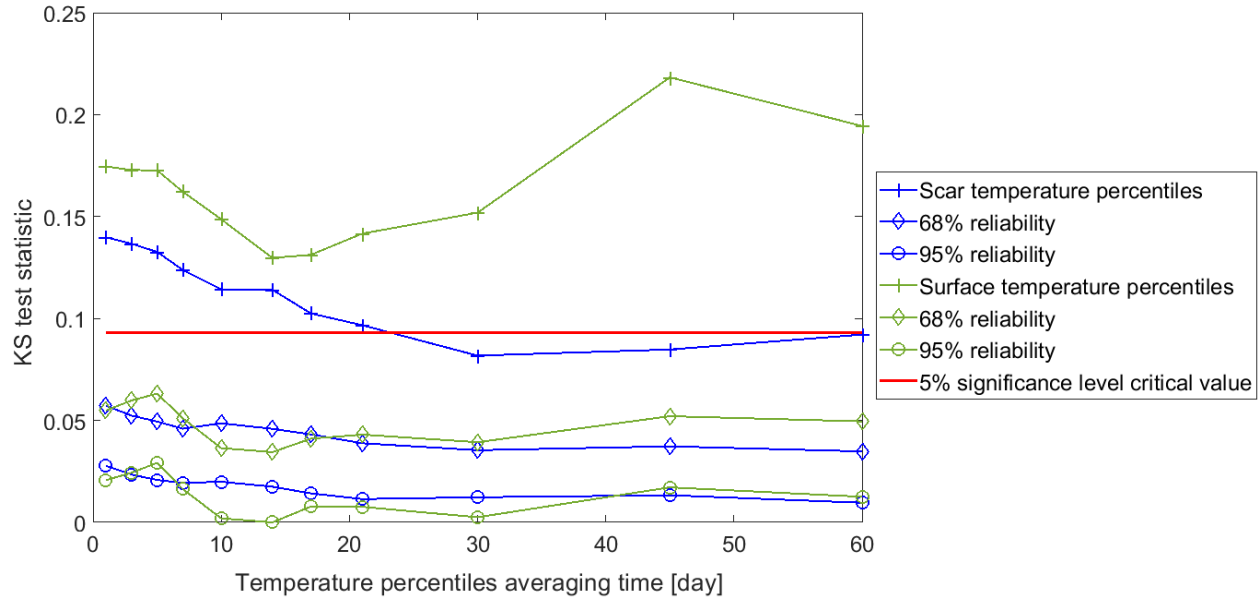
Figure 10. Illustration of the significance of scar and surface temperature percentiles for every temporality. Every point of this plot corresponds to a KS test. For example, the three values "k", "k_68" and "k_95" calculated in Figure 7 are here represented by the green triplet of points (plus-sign marker, diamond marker and circular marker) at the 1-day abscissa.

6. Discussion

6.1.Strengths and limitations of the study

For this study, we have used a homogeneous rockfall inventory which ensures direct comparability of the results and a coherent statistical analysis. The relatively simple thermal modeling approach may appear as the main limitation since it lacks of consideration for solar radiation variability through time, precipitations and wind effects, or snow deposit controls. Energy balance approaches which have been commonly used in rockwall permafrost modeling[19,55–57] would allow overcoming some of these limitations. However, by introducing a greater number of input parameters, energy balance models bear numerous sources of uncertainty, challenging its quantification[58]. In this way, our simple modeling approach combined with the availability of bedrock temperature data into

463   boreholes has the main advantage to permit a detailed uncertainty analysis of our results. In

464   addition, our approach accounts for most important parameters which are an average value of

465   incoming short-wave solar radiation and air temperature (for the MARST calculation[59]) at the

466   bedrock surface and the heat conduction at depth. Nevertheless, bedrock thermal parameters

467   (conductivity and heat capacity) have been calibrated with borehole temperature measurements

468   collected in the granitic part of the MBM while 18 (8.6 %) of the rockfalls occurred in the

469   metamorphic series. But since these series have in most cases very similar mineral composition as

470   the granitic unit[47], it is assumed that the results are marginally impacted, the variable anisotropy

471   which is not only related to lithology but also to site-specific fracturing possibly being the most

472   critical issue.

473   Another limit lies in snow deposits that may cool the bedrock surface and delay the thawing onset

474   during warm seasons[57,60] when some rockfalls occurred. Thus, the greater statistical significance

475   of rather long time period of high surface temperature prior to rockfalls may partly depict the time

476   needed for snow melt for some events. But, in parallel, snow melt or rainfalls could also accelerate

477   the thawing through water percolation into bedrock fractures[30,32]. The only possible reflection of

478   this overlooked effect in the results would be the events with rather low scar temperature

479   percentiles right before failure (Fig. 8). This means that the bedrock temperature didn't reach its

480   highest value when the failure occurred suggesting either that sudden heating is not the main

481   triggering factor or that other processes such as heat advection may have locally accelerated

482   bedrock warming. Such accelerated bedrock thawing was already suggested by former studies[19,37]

483   to explain permafrost-related rockfalls. Despite these limits, our results allow discussing possible

484   thermal processes triggering rockfalls according to scar depth and climate signal characteristics.

485

486   *6.2. Results interpretation*

487   *The role of thermal processes in rockfall triggering*

488   Variables comparison with scar depths (Fig. 8) has shown that it would have been irrelevant to

489   analyze the results based on scar depth groups. Such an analysis could have been attractive since

490   it could have been expected that scar temperature significance would have overweighted the one

491   of surface temperature. But the constantly low difference between random and real events

492   variables shows that the observed pattern is not specific to the real events and that the supposedly

493   link between scar depth and bedrock temperature pattern must be seen as the depiction of general

494   thermal conditions at rockfall locations. The decreasing average in scar variables (Fig. 8) must be

495   seen as the expected depth effect involving a delayed response to climate signals.

496   Temperature values at scar depths discriminate possible rockfall triggering processes with

497   permafrost degradation or frost-related processes strongly suggested for events > 6 m and for a

498   significant part of shallower events (3 to 6 m). On average, these events occurred in a range of

499   temperature between 0 and -2 °C and show noticeable agreement with experimental and theoretical

500   knowledge about reduced shear strength of ice-filled fractures within this temperature range[24,27].

501   In mountain environments, rockwalls are prone to instability because of extreme conditions with

502   large and sometimes sudden temperature variation, freeze and thaw cycles, as well as wet and dry

503   cycles throughout the year[29,61–64]. Frost weathering processes related to ice segregation and

504   volumetric expansion, as well as repeated freeze and thaw cycles leading to bedrock fatigue are

505   well recognized mechanisms preparing to bedrock failures by breaking rock bridges and favoring

506   fracture propagation[61,65–67]. Similarly, high thermal stress related to strong thermal oscillations is

507   also regarded as an essential factor favoring bedrock cracking due to repeated thermal contractions

508   and expansions that also affect non-periglacial rockwall, the warm days being particularly prone

509   to rockfall occurrence[39,40,68,69]. The fact that many shallow events occurred at positive rock

510   temperature but also well higher than average rock temperatures as suggested by the temperature

511   percentiles, corroborates those studies.

512   In addition to the interpretation of possible processes acting in rockfall, percentiles reveal how air

513   temperature signals contribute to their triggering. Indeed, temperature values are suited for an

514   intrinsic comparison of the rockfall sample elements, while temperature percentiles rather inform

515   about the thermal dynamics specific to each location of the rockfall sample elements. In addition,

516   percentiles are better suited for determining statistical significance.

517

518   *Link between air temperature signals and rockfall triggering*

519   Comparisons of percentile means (Fig. 9) show that the real events have, in average, a warmer

520   temperature condition prior to failure than random ones, whatever the considered temporality,

521   from 1 day to 2 months (Fig. 8 and S2). However, the difference between the real rockfall events

522   and the random rockfall events can also be a statistical "sample effect" and the questions of

523   whether and to what extent the sample could have been drawn from the model persist. This

524   question is answered by the KS test and the significance study (Fig. 10). In the following, a high

525   significance must be interpreted as an approval of the previous results, namely that the real events

526   show warmer temperature conditions than usual and that this difference is not due to a "sample

527   effect". The results show that the surface temperature percentiles between 1 day and 2 months

528   prior to failure are significantly higher than usual. More specifically, the highest significance for

529   these exceptionally high surface temperature percentiles is found 1.5 to 2 months prior to failure

530   and, in to a lesser extent, at an early time prior to the rockfall (1 to 5 days). In between these early

531   and late time periods, the statistical significance for the surface temperature percentiles decreases

532   and reaches a minimum at 2 weeks. This suggests that rockfall occurrences are favored by long-

533   lasting heatwaves (*i.e.* extended period of unusually high atmospheric heat) overtopped by a hot

534   spell (one or a few days of intense heat)[70]. This early compound can thus be interpreted as a

535   triggering effect which only reinforces a long-term high surface temperature signal. The late

536   compound becomes more relevant in relation to the statistical significance of the scar temperature

537   temporalities. Indeed, high significances of scar temperatures for short time period (< 20 days) are

538   in some ways a corollary of high percentiles of surface temperature for at least a month due to the

539   delay needed for heat diffusion. But this would mean that bedrock failures are somewhat a direct

540   response to extraordinary high temperature at depth. Such results are partly in agreement with the

541   findings from Luethi et al.[37]. This last study found that mid-sized rockfalls such as those we

542   investigated are a direct response to short-term periods of high surface temperature. The authors

543   attribute this fast reaction to accelerated bedrock thawing provoked by advective heat transfer from

544   water percolation. While this study was not accounting for the thermal dynamics at scar depth, our

545   study shows that scar depths were also affected by exceptionally high temperatures which are

546   explained by the only effect of heat conduction. It further demonstrates that this high temperature

547   at scar depth is likely a response to several weeks or months of high bedrock surface temperature.

548   It does not exclude effect of advective heat transport but suggests that heat conduction exerts a

549   predominant control. Such findings somehow remind the findings from Paranunzio et al.[36] which

550   pinpointed warm air temperature anomaly associated with a majority of rockfalls observed in the

551   Western Italian Alps. Finally, similarly to the study of Luethi et al.[37], it confirms that other thermal

552   processes than permafrost degradation are probably responsible for small size rockfalls,

553   supposedly high thermal stress due to intense temperature variation favoring bedrock failure

554   preparation.

555 These interpretations must be considered with caution since they are based on findings for which

556 the significance cannot be confirmed when considering the modeling approach uncertainty. This

557 limit draws some research outlooks that could lead to the definition of a susceptibility index of a

558 rockfall to occur according to the weather forecast.

559

560 *6.3. Outlooks*

561 Our study has shown that when considering model uncertainty, a part of our interpretation loses

562 significance as it is not clear whether the same results could have been drawn from a random

563 sample. For lowering these uncertainties and confirming/improving these results, two solutions are

564 possible.

565 The first one, which is the most challenging, is to lower the modeled temperature uncertainties

566 ($\sigma_{Cryogrid}$, σ_{MARST} or $\sigma_{anomaly}$; see sect. 3.5). $\sigma_{Cryogrid}$ could be improved by getting other borehole

567 data in order that CryoGRID2 parameters better represent the study area (boreholes in rockwalls

568 with other characteristics or in the metamorphic basement for example). σ_{MARST} could be tackled

569 by modeling the MARST with a RST sample collected in the study area rather than across the

570 entire European Alps[35,51]. Finally, $\sigma_{anomaly}$ could be improved by better defining the daily surface

571 temperature (see sect. 3.2.). RST anomaly time series could be created at the specific rockfall

572 locations by combining different meteorological parameters in a well-constrained energy balance

573 model.

574 The second solution for lowering the uncertainties would be to increase the sample size with a

575 higher number of rockfalls. This would lower the KS test critical values and the CDF uncertainties.

576 This second solution would be considered in the near future as the rockfall database will be

577 enriched with more recent events (2016-2020) which are currently under processing.

578   Additionally, with the method described in sect. 4, atmospheric warming and seasonal biases have

579   been ruled out. However, the bias linked with the rockfall locations persists. Indeed, the studied

580   locations were possibly particularly prone to instability (fracturing for example) as much as

581   rockfall dates were favorable for example. For removing this bias, random events should be chosen

582   in all the MBM, with characteristics (altitude, exposure, slope angle…) in accordance with the

583   rockfall sample characteristics. Such a study, in the continuation of this work, could result in the

584   development of a rockfall susceptibility index. This index would be defined with the values of the

585   four variables presented and, particularly, with their significances. This work of gathering all this

586   information could be done by machine learning or deep learning. Some of the real events will be

587   used in the learning process and the others for the testing step. Such a rockfall susceptibility index

588   could be a preliminary step towards a direct societal contribution of the past decade of permafrost

589   research, supporting risk mitigation and public awareness in a rapidly evolving environment.

590

591

592   **7. Conclusions**

593   In this paper, the thermal conditions and dynamics at and prior to rockfalls have been analyzed for

594   209 events inventoried in the MBM between 2007 and 2015 with 1D temperature modeling. Using

595   temperature measurements at five locations at the rock surface and into three 10-m-deep boreholes,

596   model uncertainty was quantified to refine model interpretation. Based on a random events

597   analysis approach, recent decades of atmospheric warming and seasonal biases have been

598   removed, and the statistical significance of our results was determined. The results were analyzed

599   through surface and scar depth temperature values to discriminate possible processes responsible

600   for rockfall triggering, as well as through temperature percentiles to analyze the statistical

601 significance and whether the rockfalls are a direct reaction to extreme air temperature signals.

602 Percentiles were defined in relation to 11 temporalities ranging from 1 day to 2 months. KS tests

603 were performed to determine whether our results could have been found from the random sample.

604 Our study draws the following conclusions:

605   ● Permafrost degradation may be responsible for almost all events which scar depth was >

606 6 m, and for a significant part of events occurring between 3 and 6 m depth.

607   ● For the 209 real events, the surface and scar temperature percentiles were, on average,

608 warmer than those of the random events. This difference is present for all the considered

609 temporalities. It is in order of magnitude of 3 % for scar temperature percentiles (1.5 % at least at

610 95 % reliability level) and 2.5 % for surface temperature percentiles (0.5 % at least at 95 %

611 reliability level).

612   ● KS test shows significant relationships between rockfalls and surface temperature

613 percentiles at least up to 2 months prior to failure, and scar temperature percentiles up to 3 weeks

614 before the events. At the rock surface, temporalities > 1 month have the greatest significance and

615 those of 1-5 days are also remarkable. At scar depths, the closer to the event day, the greater the

616 significance.

617   ● Significance results are interpreted as the effects of 1 to 5 days of extraordinary hot

618 weather (hot spell) acting as a triggering mechanism after > 1 month of exceptionally high air

619 temperature (long lasting heatwave), which result in high temperature at depth and sudden bedrock

620 failure.

621   ● Decrease of the scar temperature percentiles significances suggests that rockfalls are a

622 direct reaction (lasting less than 3 weeks) to exceptionally high bedrock temperature.

623   ● When considering 95 % reliability level, uncertainties are too high for concluding

624   anything about KS test significances (the three last points).

625   ● Our study also points out the interest to apply such an approach with a greater rockfall

626   sample to better define the significance levels and appears promising to develop rockfall

627   susceptibility index using weather forecast.

628

629

636

637   **9. References**

638   1. Ravanel L, Allignol F, Deline P, Gruber S, Ravello M. Rock falls in the Mont Blanc Massif
639   in 2007 and 2008. *Landslides*. 2010;7(4):493-501. doi:10.1007/s10346-010-0206-z

640   2. Haeberli W, Wegmann M, Vonder Mühll D. Slope stability problems related to glacier
641   shrinkage and permafrost degradation in the Alps. 1997;(90):407-414.

642   3. Ravanel L, Deline P, Lambiel C, Vincent C. Instability of a High Alpine Rock Ridge: the
643   Lower Arête Des Cosmiques, Mont Blanc Massif, France. *Geogr Ann Ser Phys Geogr*.
644   2013;95(1):51-66. doi:10.1111/geoa.12000

645   4. Duvillard P-A, Ravanel L, Marcer M, Schoeneich P. Recent evolution of damage to
646   infrastructure on permafrost in the French Alps. *Reg Environ Change*. Published online
647   February 11, 2019. doi:10.1007/s10113-019-01465-z

648 5. Bommer C, Institut fédéral de recherches sur la forêt la neige et le paysage (Birmensdorf).
649   *Construire sur le pergélisol: guide pratique*. Institut fédéral de recherches sur la forêt, la
650   neige et le paysage WSL; 2010.

651 6. Purdie H, Gomez C, Espiner S. Glacier recession and the changing rockfall hazard:
652   Implications for glacier tourism. *N Z Geogr*. 2015;71(3):189-202. doi:10.1111/nzg.12091

653 7. Mourey J, Marcuzzi M, Ravanel L, Pallandre F. Effects of climate change on high Alpine
654   mountain environments: Evolution of mountaineering routes in the Mont Blanc massif
655   (Western Alps) over half a century. *Arct Antarct Alp Res*. 2019;51(1):176-189.
656   doi:10.1080/15230430.2019.1612216

657 8. Huggel C, Zgraggen-Oswald S, Haeberli W, et al. The 2002 rock/ice avalanche at
658   Kolka/Karmadon, Russian Caucasus: assessment of extraordinary avalanche formation and
659   mobility, and application of QuickBird satellite imagery. *Nat Hazards Earth Syst Sci*.
660   2005;5(2):173-187. doi:https://doi.org/10.5194/nhess-5-173-2005

661 9. Carey M. Living and dying with glaciers: people's historical vulnerability to avalanches and
662   outburst floods in Peru. *Glob Planet Change*. 2005;47(2):122-134.
663   doi:10.1016/j.gloplacha.2004.10.007

664 10. Walter F, Amann F, Kos A, et al. Direct observations of a three million cubic meter rock-
665   slope collapse with almost immediate initiation of ensuing debris flows. *Geomorphology*.
666   2020;351:106933. doi:10.1016/j.geomorph.2019.106933

667 11. Allen SK, Rastner P, Arora M, Huggel C, Stoffel M. Lake outburst and debris flow disaster
668   at Kedarnath, June 2013: hydrometeorological triggering and topographic predisposition.
669   *Landslides*. 2016;13(6):1479-1491. doi:10.1007/s10346-015-0584-3

670 12. Haeberli W, Huggel C, Kääb A, et al. The Kolka-Karmadon rock/ice slide of 20 September
671   2002: an extraordinary event of historical dimensions in North Ossetia, Russian Caucasus. *J
672   Glaciol*. 2004;50(171):533-546. doi:10.3189/172756504781829710

673 13. Huggel C, Allen S, Deline P, Fischer L, Noetzli J, Ravanel L. Ice thawing, mountains
674   falling—are alpine rock slope failures increasing? *Geol Today*. 2012;28(3):98-104.
675   doi:10.1111/j.1365-2451.2012.00836.x

676 14. Fischer L, Purves RS, Huggel C, Noetzli J, Haeberli W. On the influence of topographic,
677   geological and cryospheric factors on rock avalanches and rockfalls in high-mountain areas.
678   *Nat Hazards Earth Syst Sci*. 2012;12(1):241-254. doi:https://doi.org/10.5194/nhess-12-241-
679   2012

680 15. Ravanel L, Deline P. Climate influence on rockfalls in high-Alpine steep rockwalls: The
681   north side of the Aiguilles de Chamonix (Mont Blanc massif) since the end of the 'Little Ice
682   Age.' *The Holocene*. 2011;21(2):357-365. doi:10.1177/0959683610374887

16. Deline P, Gardent M, Magnin F, Ravanel L. The Morphodynamics of the Mont Blanc Massif in a Changing Cryosphere: A Comprehensive Review. *Geogr Ann Ser Phys Geogr*. 2012;94(2):265-283. doi:10.1111/j.1468-0459.2012.00467.x

17. Allen SK, Gruber S, Owens IF. Exploring steep bedrock permafrost and its relationship with recent slope failures in the Southern Alps of New Zealand. *Permafr Periglac Process*. 2009;20(4):345-356. doi:10.1002/ppp.658

18. Allen SK, Cox SC, Owens IF. Rock avalanches and other landslides in the central Southern Alps of New Zealand: a regional study considering possible climate change impacts. *Landslides*. 2011;8(1):33-48. doi:10.1007/s10346-010-0222-z

19. Gruber S, Hoelzle M, Haeberli W. Permafrost thaw and destabilization of Alpine rock walls in the hot summer of 2003. *Geophys Res Lett*. 2004;31(13). doi:10.1029/2004GL020051

20. Ravanel L, Magnin F, Deline P. Impacts of the 2003 and 2015 summer heatwaves on permafrost-affected rock-walls in the Mont Blanc massif. *Sci Total Environ*. 2017;609:132-143. doi:10.1016/j.scitotenv.2017.07.055

21. Deline P, Broccolato M, Noetzli J, Ravanel L, Tamburini A. The December 2008 Crammont Rock Avalanche, Mont Blanc Massif Area, Italy. In: Margottini C, Canuti P, Sassa K, eds. *Landslide Science and Practice: Volume 4: Global Environmental Change*. Springer; 2013:403-408. doi:10.1007/978-3-642-31337-0_52

22. Frauenfelder R, Isaksen K, Lato MJ, Noetzli J. Ground thermal and geomechanical conditions in a permafrost-affected high-latitude rock avalanche site (Polvartinden, northern Norway). *The Cryosphere*. 2018;12(4):1531-1550. doi:https://doi.org/10.5194/tc-12-1531-2018

23. Deline P, Gruber S, Delaloye R, et al. Chapter 15 - Ice Loss and Slope Stability in High-Mountain Regions. In: Shroder JF, Haeberli W, Whiteman C, eds. *Snow and Ice-Related Hazards, Risks and Disasters*. Academic Press; 2015:521-561. doi:10.1016/B978-0-12-394849-6.00015-9

24. Krautblatter M, Funk D, Günzel FK. Why permafrost rocks become unstable: a rock–ice-mechanical model in time and space. *Earth Surf Process Landf*. 2013;38(8):876-887. doi:10.1002/esp.3374

25. Gruber S, Haeberli W. Permafrost in steep bedrock slopes and its temperature-related destabilization following climate change. *J Geophys Res Earth Surf*. 2007;112(F2). doi:10.1029/2006JF000547

26. Magnin F, Josnin J-Y, Ravanel L, Pergaud J, Pohl B, Deline P. Modelling rock wall permafrost degradation in the Mont Blanc massif from the LIA to the end of the 21st century. *The Cryosphere*. 2017;11(4):1813-1834. doi:https://doi.org/10.5194/tc-11-1813-2017

719 27. Davies MCR, Hamza O, Harris C. The effect of rise in mean annual temperature on the
720   stability of rock slopes containing ice-filled discontinuities. *Permafr Periglac Process*.
721   2001;12(1):137-144. doi:10.1002/ppp.378

722 28. Mamot P, Weber S, Schröder T, Krautblatter M. A temperature- and stress-controlled failure
723   criterion for ice-filled permafrost rock joints. *The Cryosphere*. 2018;12(10):3333-3353.
724   doi:10.5194/tc-12-3333-2018

725 29. Matsuoka N, Sakai H. Rockfall activity from an alpine cliff during thawing periods.
726   *Geomorphology*. 1999;28(3):309-328. doi:10.1016/S0169-555X(98)00116-0

727 30. Hasler A, Gruber S, Font M, Dubois A. Advective Heat Transport in Frozen Rock Clefts:
728   Conceptual Model, Laboratory Experiments and Numerical Simulation. *Permafr Periglac*
729   *Process*. 2011;22(4):378-389. doi:10.1002/ppp.737

730 31. Krautblatter M, Hauck C. Electrical resistivity tomography monitoring of permafrost in solid
731   rock walls. *J Geophys Res Earth Surf*. 2007;112(F2). doi:10.1029/2006JF000546

732 32. Phillips M, Haberkorn A, Draebing D, Krautblatter M, Rhyner H, Kenner R. Seasonally
733   intermittent water flow through deep fractures in an Alpine Rock Ridge: Gemsstock, Central
734   Swiss Alps. *Cold Reg Sci Technol*. 2016;125:117-127.
735   doi:10.1016/j.coldregions.2016.02.010

736 33. Krautblatter M, Huggel C, Deline P, Hasler A. Research Perspectives on Unstable High-
737   alpine Bedrock Permafrost: Measurement, Modelling and Process Understanding. *Permafr*
738   *Periglac Process*. 2012;23(1):80-88. doi:10.1002/ppp.740

739 34. Fischer L, Amann F, Moore JR, Huggel C. Assessment of periglacial slope stability for the
740   1988 Tschierva rock avalanche (Piz Morteratsch, Switzerland). *Eng Geol*. 2010;116(1):32-
741   43. doi:10.1016/j.enggeo.2010.07.005

742 35. Magnin F, Brenning A, Bodin X, Deline P, Ravanel L. Statistical modelling of rock wall
743   permafrost distribution: application to the Mont Blanc massif. *Géomorphologie Relief*
744   *Process Environ*. Published online 2015:20.

745 36. Paranunzio R, Laio F, Chiarle M, Nigrelli G, Guzzetti F. Climate anomalies associated with
746   the occurrence of rockfalls athigh-elevation in the Italian Alps. *Nat Hazards Earth Syst Sci*.
747   2016;16(9):2085-2106. doi:10.5194/nhess-16-2085-2016

748 37. Luethi R, Gruber S, Ravanel L. Modelling transient ground surface temperatures of past
749   rockfall events: towards a better understanding of failure mechanisms in changing periglacial
750   environments. *Geogr Ann Ser Phys Geogr*. 2015;97(4):753-767. doi:10.1111/geoa.12114

751 38. Allen S, Huggel C. Extremely warm temperatures as a potential cause of recent high
752   mountain rockfall. *Glob Planet Change*. 2013;107:59-69.
753   doi:10.1016/j.gloplacha.2013.04.007

754 39. Bakun-Mazor D, Keissar Y, Feldheim A, Detournay C, Hatzor YH. Thermally-Induced
755   Wedging–Ratcheting Failure Mechanism in Rock Slopes. *Rock Mech Rock Eng*.
756   2020;53(6):2521-2538. doi:10.1007/s00603-020-02075-6

757 40. Collins BD, Stock GM. Rockfall triggering by cyclic thermal stressing of exfoliation
758   fractures. *Nat Geosci*. 2016;9(5):395-400. doi:10.1038/ngeo2686

759 41. Hugentobler M, Loew S, Aaron J, Roques C, Oestreicher N. Borehole monitoring of thermo-
760   hydro-mechanical rock slope processes adjacent to an actively retreating glacier.
761   *Geomorphology*. 2020;362:107190. doi:10.1016/j.geomorph.2020.107190

762 42. Westermann S, Schuler TV, Gisnås K, Etzelmüller B. Transient thermal modeling of
763   permafrost conditions in Southern Norway. *The Cryosphere*. 2013;7(2):719-739.
764   doi:10.5194/tc-7-719-2013

765 43. Schär C, Vidale PL, Lüthi D, et al. The role of increasing temperature variability in
766   European summer heatwaves. *Nature*. 2004;427(6972):332-336. doi:10.1038/nature02300

767 44. Gobiet A, Kotlarski S, Beniston M, Heinrich G, Rajczak J, Stoffel M. 21st century climate
768   change in the European Alps—A review. *Sci Total Environ*. 2014;493:1138-1151.
769   doi:10.1016/j.scitotenv.2013.07.050

770 45. Christidis N, Jones GS, Stott PA. Dramatically increasing chance of extremely hot summers
771   since the 2003 European heatwave. *Nat Clim Change*. 2015;5(1):46-50.
772   doi:10.1038/nclimate2468

773 46. Haeberli W, Noetzli J, Arenson L, et al. Mountain permafrost: development and challenges
774   of a young research field. *J Glaciol*. 2010;56(200):1043-1058.
775   doi:10.3189/002214311796406121

776 47. von Raumer JF, Bussy F. *Mont Blanc and Aiguilles Rouges Geology of Their
777   Polymetamorphic Basement (External Massifs, Western Alps, France-Switzerland)*. Section
778   des Sciences de la Terre, Université de Lausanne; 2004:218.
779   https://www.unil.ch/iste/files/live/sites/iste/files/shared/X.Library/Memoirs%20of%20Geolo
780   gy/42%20-%20Von%20Raumer%20%26%20Bussy%20(2004%20-
781   %20entire%20volume).pdf

782 48. Gardent M, Rabatel A, Dedieu J-P, Deline P. Multitemporal glacier inventory of the French
783   Alps from the late 1960s to the late 2000s. *Glob Planet Change*. 2014;120:24-37.
784   doi:10.1016/j.gloplacha.2014.05.004

785 49. Magnin F, Deline P, Ravanel L, Noetzli J, Pogliotti P. Thermal characteristics of permafrost
786   in the steep alpine rock walls of the Aiguille du Midi (Mont Blanc Massif, 3842 m a.s.l). *The
787   Cryosphere*. 2015;9(1):109-121. doi:10.5194/tc-9-109-2015

788 50. Ravanel L, Deline P. A network of observers in the Mont Blanc massif to study rockfalls in
789   high alpine rockwalls. *Geogr Fis E Din Quat*. 2013;(36):151-158.

790   51. Boeckli L, Brenning A, Gruber S, Noetzli J. A statistical approach to modelling permafrost
791   distribution in the European Alps or similar mountain ranges. *The Cryosphere*.
792   2012;6(1):125-140. doi:10.5194/tc-6-125-2012

793   52. Hasler A, Gruber S, Haeberli W. Temperature variability and offset in steep alpine rock and
794   ice faces. *The Cryosphere*. 2011;5(4):977-988. doi:https://doi.org/10.5194/tc-5-977-2011

795   53. Noetzli J, Gruber S, Kohl T, Salzmann N, Haeberli W. Three-dimensional distribution and
796   evolution of permafrost temperatures in idealized high-mountain topography. *J Geophys Res
797   Earth Surf*. 2007;112(F2). doi:10.1029/2006JF000545

798   54. Rolland C. Spatial and Seasonal Variations of Air Temperature Lapse Rates in Alpine
799   Regions. *J Clim*. 2003;16(7):1032-1046. doi:10.1175/1520-
800   0442(2003)016<1032:SASVOA>2.0.CO;2

801   55. Noetzli J, Gruber S, Kohl T, Salzmann N, Haeberli W. Three-dimensional distribution and
802   evolution of permafrost temperatures in idealized high-mountain topography. *J Geophys Res*.
803   2007;112(F2):F02S13. doi:10.1029/2006JF000545

804   56. Luethi R, Gruber S, Ravanel L. Modelling transient ground surface temperatures of past
805   rockfall events: towards a better understanding of failure mechanisms in changing periglacial
806   environments. *Geogr Ann Ser Phys Geogr*. 2015;97(4):753-767. doi:10.1111/geoa.12114

807   57. Magnin F, Westermann S, Pogliotti P, Ravanel L, Deline P, Malet E. Snow control on active
808   layer thickness in steep alpine rock walls (Aiguille du Midi, 3842ma.s.l., Mont Blanc
809   massif). *CATENA*. 2017;149:648-662. doi:10.1016/j.catena.2016.06.006

810   58. Loucks DP, Beek E van, Stedinger JR. *Water Resources Systems Planning and
811   Management: An Introduction to Methods, Models and Applications*. UNESCO; 2005.

812   59. Magnin F, Brenning A, Bodin X, Deline P, Ravanel L. Modélisation statistique de la
813   distribution du permafrost de paroi : application au massif du Mont Blanc. *Géomorphologie
814   Relief Process Environ*. 2015;21(vol. 21 – n° 2):145-162.
815   doi:10.4000/geomorphologie.10965

816   60. Magnin F, Deline P, Ravanel L, Noetzli J, Pogliotti P. Thermal characteristics of permafrost
817   in the steep alpine rock walls of the Aiguille du Midi (Mont Blanc Massif, 3842 m a.s.l). *The
818   Cryosphere*. 2015;9(1):109-121. doi:https://doi.org/10.5194/tc-9-109-2015

819   61. Hall K. The role of thermal stress fatigue in the breakdown of rock in cold regions.
820   *Geomorphology*. 1999;31(1-4):47-63. doi:10.1016/S0169-555X(99)00072-0

821   62. Sass O. Rock Moisture Fluctuations During Freeze-thaw Cycles: Preliminary Results from
822   Electrical Resistivity Measurements. *Polar Geogr*. 2004;28(1):13-31.
823   doi:10.1080/789610157

824   63. Matsuoka N. Direct observation of frost wedging in alpine bedrock. *Earth Surf Process
825   Landf*. 2001;26(6):601-614. doi:10.1002/esp.208

826 64. McColl ST, Draebing D. Rock Slope Instability in the Proglacial Zone: State of the Art. In:
827   Heckmann T, Morche D, eds. *Geomorphology of Proglacial Systems: Landform and*
828   *Sediment Dynamics in Recently Deglaciated Alpine Landscapes*. Geography of the Physical
829   Environment. Springer International Publishing; 2019:119-141. doi:10.1007/978-3-319-
830   94184-4_8

831 65. Matsuoka N, Murton J. Frost weathering: recent advances and future directions. *Permafr*
832   *Periglac Process*. 2008;19(2):195-210. doi:10.1002/ppp.620

833 66. Draebing D, Krautblatter M. The Efficacy of Frost Weathering Processes in Alpine
834   Rockwalls. *Geophys Res Lett*. 2019;46(12):6516-6524. doi:10.1029/2019GL081981

835 67. Jia H, Xiang W, Krautblatter M. Quantifying Rock Fatigue and Decreasing Compressive and
836   Tensile Strength after Repeated Freeze-Thaw Cycles. *Permafr Periglac Process*.
837   2015;26(4):368-377. doi:10.1002/ppp.1857

838 68. Vargas EAJr, Veloso RQ, Chavez LE, Gusmão L, Amaral CP. On the Effect of Thermally
839   Induced Stresses in Failures of Some Rock Slopes in Rio de Janeiro, Brazil.
840   *springerprofessional.de*. 2012;46:123-134.

841 69. Gunzburger Y, Merrien-Soukatchoff V, Guglielmi Y. Influence of daily surface temperature
842   fluctuations on rock slope stability: case study of the Rochers de Valabres slope (France). *Int*
843   *J Rock Mech Min Sci*. 2005;3(42):331-349. doi:10.1016/j.ijrmms.2004.11.003

844 70. Robinson PJ. On the Definition of a Heat Wave. *J Appl Meteorol*. 2001;40(4):762-775.
845   doi:10.1175/1520-0450(2001)040<0762:OTDOAH>2.0.CO;2

846

847   **Table 1.** Summary characteristics of the 209 rockfall events used in this study. MARST refers to the

848   Mean Annual Rock Surface Temperature such as displayed in Figure 1.

	Altitude (m)	MARST (°C)	Volume (m^3)	Scar depth (m)	Slope angle (°)
Minimum	2175	-8.7	100	0.8	12*
Mean	3341	-2	1836	3	57
Median	3355	-2	400	3.8	57
Maximum	4085	4	60 000	15	82

849

850   **Table 1:** Optimum parameters for minimizing the RMSE between simulated and real borehole temperatures. * This

851   low value is explained by the fact that the rockfall occurred from the top of a crest.

Parameter	Value
Bedrock conductivity ($k_{bedrock}$)	3.3 W.m^{-1}.K^{-1}
Bedrock porosity (φ)	1 %
Total water content ($\theta_{w,tot}$)	1 %
Bedrock volumetric heat capacity	2.10^6 J.m^{-3}.K^{-1}
Profile resolution	From 1 to 3 m: 0.1 m From 3 to 10 m: 0.2 m From 10 m to 20.5 m: 0.5 m
Spin-up duration	3 years
C_{exp}	4

852